Ultra-lightweight anthropomorphic dual-arm rolling robot for dexterous manipulation tasks on linear infrastructures: A self-stabilizing system ☆

Alejandro Suarez [*], Saeed Rafee Nekoo, Anibal Ollero

GRVC Robotics Labs, Universidad de Sevilla. Camino de los Descubrimientos s/n, 41092, Seville, Spain[1]

ARTICLE INFO

ABSTRACT

This paper proposes the application of a very low weight (3.2 kg) anthropomorphic dual-arm system capable of rolling along linear infrastructures such as power lines to perform dexterous and bimanual manipulation tasks like the installation of clip-type bird flight diverters or conduct contact-based inspection operations on pipelines to detect corrosion or leaks. The kinematic configuration of the arms, with three joints at the shoulder and one at the elbow, allows the natural replication of the human movements to conduct these tasks, exploiting also the kinematic redundancy of the shoulder to maintain the equilibrium while perching on the line. The dynamic model of the system is derived to design a self-stabilizing controller that maintains the base of the arms at an equilibrium point. The state-dependent Riccati equation (SDRE) controller is chosen for this purpose since the system is under-actuated and the contribution of the control gain (with nonlinear optimal structure) on all states is critical. The SDRE is a nonlinear optimal controller that extends the margins of stability in comparison with linear ones. Simulation results show that the SDRE performs the regulation to the equilibrium point successfully and evidence better performance with respect to a linear quadratic regulator (LQR). The system is validated in an outdoor testbed consisting of a power line mockup, presenting experimental results to evaluate the SDRE and LQR controllers, demonstrating also the autonomous installation of clip-type bird flight diverters and the aerial deployment using a multirotor platform.

1. Introduction

Replicating the bimanual manipulation skills of human workers facilitates the implementation of advanced robotic functionalities for inspection and maintenance applications, taking into account that most of the current procedures and devices employed are intended for human operators. However, the transportation, handling, and deployment of robotic systems in high-altitude infrastructures such as power lines or pipe structures in chemical plants become difficult when the weight of the robot is in the range of tens or hundreds of kilograms. In this sense, aerial robots with manipulation capabilities [1,2] are particularly suitable for operating in this kind of scenario given their ability to reach quickly and hover in high-altitude workspaces to conduct the operation. Despite the evident benefits of multirotor platforms, the limited flight time and the relatively low positioning accuracy in outdoor experiments (considering also the effect of wind gusts and physical interactions on a flight) are currently the main inconveniences for long-term and accurate inspection and maintenance operations. In order to overcome these inconveniences, other solutions arise, like

perching [3–6] or landing [7,8] the aerial robot on the infrastructure, or deploying the robot using the aerial platform for its transportation [9]. This requires the development of very low-weight manipulators that provide a certain level of dexterity to conduct operations with devices or tools, as the prototype developed in this work and shown in Fig. 1. Mechanical joint compliance is also a highly desirable feature for the manipulator when conducting operations involving physical interactions with the environment [10,11], particularly when impulsive forces (impacts) are involved. However, the flexibility of the joints may cause significant position errors and overshoot at the end effector that become more evident as the payload increases, which motivates the design of appropriate control methods [12,13].

1.1. Power line inspection robots

The power grid is a critical infrastructure in any country, requiring periodic maintenance to ensure continuous service due to its exposition to adverse outdoor environmental conditions, affected by the

---

Fig. 1. Lightweight and compliant, anthropomorphic dual-arm rolling robot installing clip-type bird flight diverters on a power line.

climate, vegetation, and bird species. Conventional maintenance methods [14] are carried out by human workers, involving a significant risk due to the high altitude and high voltage. Given its vast extension, and taking into account the interest in reducing the risk and cost of the inspection and maintenance operation, several robotic solutions have been proposed for this purpose [15,16]. A classification in three groups according to the locomotion method was proposed [15]: climbing/rolling [17–19], flying [20–23], and hybrid climbing-flying [24–26]. The first group comprises platforms capable of rolling along with the aluminum conductors with lower energy consumption compared w.r.t. (with respect to) flying platforms, integrating specific sensor devices for detecting defects on the aluminum cables [19]. Articulated limbs, similar to arms, are used for avoiding obstacles along the power line like electrical spacers, insulators, or markers, at the expense of increasing the weight of the robot, which may vary between 8 and 100 kg [15]. This factor should be taken into account as it determines the complexity and effort required by the operators to deploy the robot on the line [14].

Multirotor and unmanned helicopters [27,28] are particularly suitable platforms to conduct power line inspection [22] and maintenance [21,29] operations due to the considerable reduction in time and risk for reaching the point of interest w.r.t conventional procedures. Note that most flying robots developed in past years are designed to perform only inspection operations, carrying visual or thermal cameras for detecting faults, or 3D lasers for estimating vegetation growth [16, 17]. However, the realization of maintenance tasks requires the physical interaction of the aerial robot with the power line. In the context of the AERIAL-CORE (AERIAL COgnitive integrated multi-task Robotic system with Extended operation range and safety) project in which this work is developed, some prototypes have been proposed to install devices like bird flight diverters or electrical spacers [30].

1.2. Pipelines inspection robots

Contact or visual-based inspection methods are frequently carried out to detect corrosion or leaks in extensive pipe structures typical of oil and gas refineries [31] or in many chemical plants. As occurs with the power lines, human workers need to climb or require the support of elevated working platforms to reach the points of interest due to the high altitude of these structures. In some cases, the pipes may not be even accessible due to the presence of obstacles or because they are covered by walls. This motivated the early interest [32] in the design and development of diverse robot prototypes for in-pipe inspection [33], with the focus on reliability aspects of the locomotion mechanism [34]. Two relevant inconveniences are derived from in-pipe inspection in large infrastructures. On the one hand, the robot has to be introduced into the pipe through available access points [35] that may be far away from the point of interest. On the other hand, and related to the previous point, there is a certain risk that the robot gets stuck or

runs out of battery while crawling, so recovering the robot may become a problem.

The advances in sensing technology for measuring material thickness based on Eddy currents with non-destructive testing [36] has facilitated the realization of inspection operations in pipe structures [37], consisting basically in placing the sensor probe in the point of interest. Again, aerial robots have been considered for inspection and maintenance of this kind of infrastructure, demonstrating their capabilities in representative scenarios like oil and gas refineries [38]. Interaction force control with a pipe structure has been evaluated on a flight in [10] relying on the mechanical joint compliance of the dual arm manipulator and an on-board perception system that measures the Cartesian deflection. More recently, hybrid rolling-aerial robots with manipulation capabilities have been proposed [7,8], taking advantage of both locomotion methods while exploiting the dexterity of the robotic arm to access different locations of a pipe array. The design of the rolling base presents some difficulties and inconveniences in terms of weight and maneuverability since it has to support the weight of the overall robot, contributing at the same time to decreasing the effective payload capacity and flight time of the aerial platform.

1.3. Stabilizing systems on linear infrastructures

The lack of stable support points on power lines or pipelines makes it necessary for the robot to maintain equilibrium while operating on the linear infrastructure. The system can be assimilated to a normal or inverted pendulum depending on whether the center of mass is above or below the contact point of the wheeled base, resulting in under-actuated dynamics since the perching mechanism is assimilated to a passive joint. This raises the formulation of a control problem for the stabilization of the base of the robot using the actuated joints. Among the different approaches for controlling these kinds of systems, the state-dependant Riccati equation (SDRE) controller stands out because it mimics the linear quadratic regulator (LQR) though with a nonlinear form and has been reported as an effective controller for pendulum-like systems and stabilizers [39,40]. The LQR proposes a trade-off between the error and energy consumption in a quadratic cost function [41, 42]. The SDRE is a nonlinear sub-optimal controller, introduced in the 1960s [43], and extended and applied in various works such as stabilization of pendulums [44,45], propeller-type pendulum [46,47], unmanned aerial vehicles [48,49], or the control of flexible joint manipulators [13]. The under-actuation in the control systems prevents the designer from implementing classical straightforward controllers. The state-space-based methods such as LQR and SDRE are helpful since the control signal benefits from all state-feedback variables and is updated by the optimal control law. Huifeng et al. [50] presented the swinging-up and stabilization of an inverted pendulum using the SDRE controller.

1.4. Main contribution and novelties

This paper presents a very low-weight (3.2 kg) anthropomorphic dual-arm system with a rolling base intended to conduct inspection and maintenance operations on linear infrastructures like power lines or pipelines, exploiting the kinematic redundancy of the shoulder joints of the left and right arms to stabilize the base of the robot while perching or rolling. Relying on the derived dynamic model of the system, a self-stabilizing controller is proposed based on the state-dependent Riccati equation (SDRE) to correct deviations in the orientation of the manipulator due to unbalanced mass distributions, after its deployment on the infrastructure, or due to perturbations caused by the wind or forces exerted during the operation. The under-actuation problem is controlled through the proper definition of the weighting matrix for states that distributes the importance of state variables. The human size and human-like kinematic configuration of the arms, with four joints

for end-effector positioning, allows the realization of bimanual manipulation tasks and extends the effective workspace w.r.t. a single-arm manipulator. The lightweight design allows the system to be integrated into multirotor platforms for aerial transportation and deployment, facilitating access to high-altitude workspaces like the ones considered in this work. Experimental results in a mockup indoor/outdoor testbed validate the system design and intended applications.

The presented system is an evolution of our previous works [7,10, 11,47,51,52], remarking the following novelties:

- The manipulator is intended to operate in perching or rolling conditions, not on the flight, avoiding in this way the limitations of the aerial platform in terms of flight time, positioning accuracy, and dynamic coupling.
- The multirotor platform is used for the transportation, deployment, and retrieval of the manipulator.
- The shoulder structure of the arms incorporates a rolling mechanism and an inertial measurement unit (IMU) to measure and control the orientation in the roll angle of the base when deployed on the linear infrastructure.
- The SDRE controller is specifically designed and implemented taking into account the characterization of the smart servo actuators employed on the robotic arms.
- The MATLAB Riccati solver, "care" command, has been usually used for implementation of the SDRE in the literature [46,47], though, in this work, the Schur decomposition was implemented in C language using LAPACK library, allowing its execution in real time (around 1 ms computation time) on a Raspberry Pi computer board.

The rest of the paper is organized as follows. An application overview is presented in Section 2. Section 3 derives the kinematic and dynamic models, whereas Section 4 is focused on the controller design. Section 5 describes the developed prototype and its integration in a multirotor platform. Simulation and experimental results are reported in Section 6, summarizing the conclusions of this work in Section 7.

2. Applications overview

The anthropomorphic dual-arm rolling robot presented in this work is intended to conduct inspection and maintenance operations on linear infrastructures like power lines [21,29] or pipe structures in chemical plants [7,11], using a multirotor aerial platform for fast transportation, deployment, and retrieval to the ground base, avoiding in this way the risk for the human workers associated to the high altitude and difficult access of these scenarios. Two typical inspection and maintenance operations that involve a significant time due to the vast extension of these infrastructures can be considered:

1. The installation of clip-type bird diverters [29,53], a bimanual manipulation operation in which one arm holds the device with one arm around the power line, while the other removes a lock of the clamp mechanism.
2. The visual or contact-based inspection of the contours of a pipe [7,8] to detect possible corrosion or leaks, using the left and right arms to place the sensor device at both sides and the bottom of the pipe.

Fig. 2 illustrates the aerial transportation and deployment of the dual-arm rolling robot, remarking on the similarities in both infrastructures. For example, the approaching and deployment of the arms with the multirotor are carried out from above and not from below due to the risk of collision with the pipes [7] or electrostatic discharge when the aerial robot (considered as a floating conductor) is flying between two high voltage lines [21]. Also, these linear infrastructures do not provide stable support points for the robot, which can be assimilated
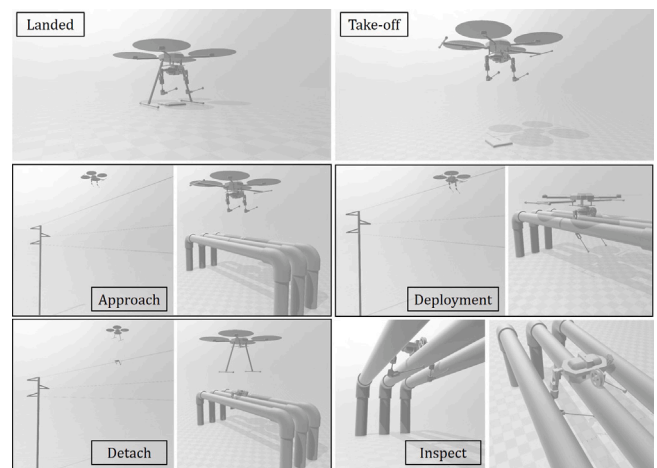

Fig. 2. Phases involved in the aerial deployment of the dual-arm rolling robot on a power line and a pipe structure using a multirotor platform. In both cases, the approaching and deployment maneuvers are carried out from above to prevent collisions with the infrastructure.

to a pendulum, which motivates the design and implementation of a self-stabilizing system [47].

Protecting birds against collisions and electrocution with the power lines is a relevant task carried out by the companies responsible for the maintenance of the power grid due to local or national regulations. The installation of clip-type (Fig. 1) or helical bird flight diverters [29], is a common solution that involves significant risk for the human workers since the operation is carried out on live power lines at tens or hundreds of kilo Volts and high altitudes between 15 to 50 m. Access to this kind of workspaces, either climbing, using elevated work platforms, or manned helicopters [14,53], requires following strict safety protocols for the workers [21], which tends to reduce the effective operation time and increase the effort.

Unlike the in-pipe inspection robots previously mentioned, the dual-arm manipulator developed here can be directly deployed at the desired inspection area without the need to crawl from an access point, but using the multirotor aerial platform for this purpose. The kinematic configuration and symmetry of the dual-arm system can be exploited to reach the points of interest in single pipes or pipe arrays, as shown in Fig. 2, as long as the gap between the pipes is big enough to introduce the arms between them [7]. The end-effector of the arms can be equipped with visual or contact sensors to obtain the inspection measurements, relying on the mechanical joint compliance of the arms [10,11,51] to support the contact forces raised during the physical interaction with the pipe.

In both applications, the installation or inspection operation is typically repeated at different points along with the linear infrastructure, so the robot should be able to roll along with it. In this sense, detaching the dual arm from the aerial platform presents two relevant benefits. On the one hand, the required torque, weight, and energy consumption of the rolling platform are lower than in [7], achieving also higher speeds. On the other hand, the center of mass of the robot is closer to the contact point of the rolling base, preventing inverted pendulum configurations that tend to destabilize the system.

Given the similarities in the aerial deployment and control of the dual arm manipulator in both types of infrastructures, and taking into account that in our previous work we considered already the pipe structures [7,10,11,47], in the following we will focus on the application to power lines.

3. Modeling

This section describes the kinematics and dynamics of the dual-arm rolling robot. The complete 3D kinematic model of the arms is firstly
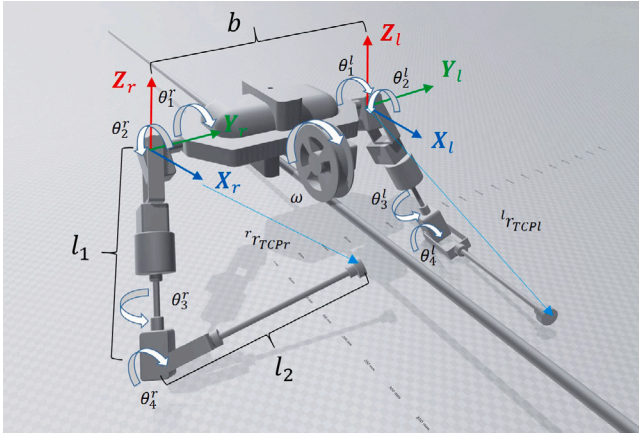
Fig. 3. Kinematic model of the anthropomorphic dual-arm rolling robot operating on a linear infrastructure.

introduced in Section 3.1 since it is necessary for implementing the manipulation task, whereas the design of the self-stabilizing system, one of the main contributions of this paper, relies on the planar 2D model presented in Section 3.2. Note that the control problem addressed in Section 4 is formulated in the plane perpendicular to the line of the infrastructure.

3.1. Anthropomorphic dual-arm kinematics

Motivated by the convenience of replicating the dexterous and bimanual manipulation capabilities of the human workers, the dual-arm system developed in this work implements the anthropomorphic kinematic configuration described in [51] and depicted in Fig. 3, providing four degrees of freedom (DoF) for end-effector positioning. Denoting by θ_j^i the rotation angle of the jth joint of the ith arm, these are:

- Shoulder flexion/extension (θ_1^i).
- Shoulder adduction/abduction (θ_2^i)
- Lateral/medial rotation (θ_3^i)
- Elbow flexion/extension (θ_4^i)

with $i = \{l, r\}$ for the left/right arms. Wrist orientation joints are not considered since these depend on the particular requirements of each task and because it is preferable to reduce the weight and inertia of the arms as much as possible. The separation distance between the left/right arms is b, whereas l_1 and l_2 are the upper arms and forearm links length.

The manipulation task conducted by each arm is defined as a trajectory or sequence of positions of the end-effector relative to its reference frame $\{X_iY_iZ_i\}$, whose origin is at the intersection of the shoulder rotation axes, with the X-axis pointing forwards, and the Z-axis pointing upwards. If $\mathbf{r}_{TCPi}^i = [x_i, y_i, z_i]^\top$ and $\theta^i = [\theta_1^i, \theta_2^i, \theta_3^i, \theta_4^i]^\top$ are the end-effector and joint position vectors, respectively, then the forward/inverse kinematic models are defined as:

$$\mathbf{r}_{TCPi}^i = \mathbf{FK}^i(\theta^i) \;\; ; \;\; \theta^i = \mathbf{IK}^i(\mathbf{r}_{TCPi}^i, \varphi_i) \tag{1}$$

where $\varphi_i = \theta_2^i$ is taken as a parameter for solving the kinematic redundancy of the arms in the $\mathbb{R}^3 \rightarrow \mathbb{R}^4$ mapping. This joint will be used for the self-stabilizing system for maintaining the equilibrium of the linear infrastructure. The analytical solution of the forward and inverse kinematics can be found in [51].

Finally, the shoulder structure incorporates a rolling base consisting of a continuous rotation servo whose angular speed ω can be directly controlled, and a wheel of radius R, so the linear velocity of the robot is $v = R\omega$. Table 1 indicates the value of the different parameters of the dual-arm rolling robot.

Table 1
Parameters of the dual-arm rolling robot.

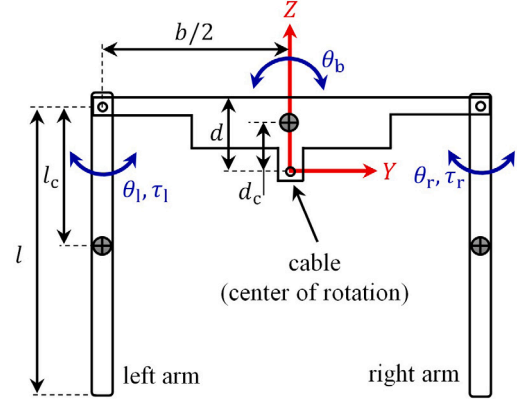| Parameter	Value	Unit
l_1	250	mm
l_2	250	mm
b	360	mm
ω	[−250, 250]	deg/s
R	0.03	m
v	[−0.14, 0.14]	m/s

Fig. 4. A schematic model of the stabilizer system.

3.2. Kinematics of the pendulum system

As stated in the previous section, linear infrastructures like the power grid or pipelines do not provide stable support for the rolling base, so the robot will have to exploit its kinematic redundancy to maintain equilibrium while perching on the line. To perform the required control task (described in Section 4), a mathematical model is considered, as shown in Fig. 4. The shoulder roll angle of both arms, $\theta_l = \theta_2^1$ and $\theta_r = \theta_2^2$, are devoted to the stabilization of the platform over the cable, which can be seen as regulation of θ_b to zero. In the following, it is assumed that in this planar configuration the rotation angle of the other shoulder joints is set to zero, and the elbow joint is rotated 90 deg to lift the arms in the L-shaped pose. Note that the base may be destabilized due to unbalanced mass distributions, due to wind gusts, the downwash effect during the deployment, or the realization of manipulation tasks. The kinematic redundancy of the arms, with four joints for end-effector positioning, allows conducting the task without having control over θ_r and θ_l, exploiting the symmetry of the platform w.r.t. Z-axis.

The generalized coordinates and their time derivatives of the stabilizer system are firstly defined as:

$$\mathbf{q}(t) = [\theta_b(t), \theta_r(t), \theta_l(t)]^\top \tag{2}$$

$$\dot{\mathbf{q}}(t) = [\dot{\theta}_b(t), \dot{\theta}_r(t), \dot{\theta}_l(t)]^\top \tag{3}$$

The center of mass of the body, left and right arms are defined as follows considering the right-hand sign criteria:

$$y_{c,b} = -d_c sin(\theta_b), \tag{4}$$

$$z_{c,b} = d_c cos(\theta_b), \tag{5}$$

$$y_{c,r} = -d sin(\theta_b) + \frac{b}{2} cos(\theta_b) + l_c cos(\theta_b - \frac{\pi}{2} + \theta_r), \tag{6}$$

$$z_{c,r} = d cos(\theta_b) + \frac{b}{2} sin(\theta_b) + l_c sin(\theta_b - \frac{\pi}{2} + \theta_r), \tag{7}$$

$$y_{c,l} = -d sin(\theta_b) - \frac{b}{2} cos(\theta_b) + l_c cos(\theta_b - \frac{\pi}{2} + \theta_l), \tag{8}$$

Table 2
The parameters of the stabilizer system.

Parameters	Value	Unit	Source
m_b	1.8	kg	Measured
m_r, m_l	0.6	kg	Measured
I_b	0.0159	kg m^2	Computed
I_r, I_l	0.0035	kg m^2	Computed
b	0.36	m	Measured
d	0.05	m	Measured
d_c	0.03	m	Computed
l	0.175	m	Measured
l_c	0.124	m	Computed
d_b, d_r, d_l	0.05, 0.5, 0.5	kg m/s	Estimated

$$z_{c,l} = dcos(\theta_b) + \frac{b}{2}sin(\theta_b) + l_c sin(\theta_b - \frac{\pi}{2} + \theta_l), \quad (9)$$

where d is the height of the body link from the cable, b is the width of the platform, l is the length of the left and right links, and the index "c" stands for center of mass in the parameters, whereas "l" and "r" denote left and right arms. The parameters of the system are indicated in Table 2.

3.3. Dynamics of the pendulum system

The dynamic model of the equivalent pendulum system, shown in Fig. 4, can be derived from the Lagrangian and the generalized equation of the forces and moments:

$$\frac{d}{dt}\left\{\frac{\partial \mathcal{L}}{\partial \dot{\mathbf{q}}}\right\} - \left\{\frac{\partial \mathcal{L}}{\partial \mathbf{q}}\right\} = \tau + \tau_f, \quad (10)$$

where $\mathcal{L} = K - V$ is the Lagrangian, K, and V are the kinetic and potential energy, respectively, τ is the torque vector, and τ_f is the friction vector. The kinetic energy is the sum of the contribution of the three bodies: the main body m_b, I_b, left arm m_l, I_l and right arm m_r, I_r, whose positions are given in the previous subsection. The kinetic energy is then defined:

$$K = \frac{1}{2}\left(m_b(\dot{y}_{c,b}^2 + \dot{z}_{c,b}^2) + m_r(\dot{y}_{c,r}^2 + \dot{z}_{c,r}^2) + m_l(\dot{y}_{c,l}^2 + \dot{z}_{c,l}^2) + I_b\dot{\theta}_b^2 + I_r(\dot{\theta}_b + \dot{\theta}_r)^2 + I_l(\dot{\theta}_b + \dot{\theta}_l)^2\right), \quad (11)$$

and the potential energy is computed as follows:

$$V = g(m_b z_{b,c} + m_r z_{r,c} + m_l z_{l,c}), \quad (12)$$

in which g [m/s^2] is the gravity constant. Combining Eqs. (10)–(12), the equation of motion (EoM) of the system can be expressed in the matrix form:

$$\mathbf{M}(\mathbf{q})\ddot{\mathbf{q}} + \mathbf{c}(\mathbf{q}, \dot{\mathbf{q}}) + \mathbf{g}(\mathbf{q}) = \mathbf{E}\tau + \tau_f, \quad (13)$$

where $\mathbf{M}(\mathbf{q}): \mathbb{R}^3 \rightarrow \mathbb{R}^{3\times3}$ is the generalized mass matrix, $\mathbf{c}(\mathbf{q}, \dot{\mathbf{q}}): \mathbb{R}^3 \times \mathbb{R}^3 \rightarrow \mathbb{R}^3$ represents the centrifugal and Coriolis terms, and $\mathbf{g}(\mathbf{q}): \mathbb{R}^3 \rightarrow \mathbb{R}^3$ is the gravity vector. The friction torque can be approximated as follows:

$$\tau_f = diag(d_b, \ d_r, \ d_l)\dot{\mathbf{q}}, \quad (14)$$

where d_i is viscus friction constant for $i = \{b, r, l\}$. The EoM matrices are detailed below:

$$\mathbf{M}(\mathbf{q}) = \begin{bmatrix} m_{11}(\mathbf{q}) & m_{12}(\mathbf{q}) & m_{13}(\mathbf{q}) \\ m_{12}(\mathbf{q}) & m_r l_{c,r}^2 + I_r & 0 \\ m_{13}(\mathbf{q}) & 0 & m_l l_{c,l}^2 + I_l \end{bmatrix}, \quad (15)$$

$$\mathbf{c}(\mathbf{q}, \dot{\mathbf{q}}) = \begin{bmatrix} c_1(\mathbf{q}, \dot{\mathbf{q}}) \\ -\frac{\theta_b^2 l_c m_r(bcos(\theta_r)+2dsin(\theta_r))}{2} \\ -\frac{\theta_b^2 l_c m_l(bcos(\theta_l)-2dsin(\theta_l))}{2} \end{bmatrix}, \quad (16)$$

$$\mathbf{q}(\mathbf{q}) = \begin{bmatrix} g_1(\mathbf{q}) \\ gl_c m_r sin(\theta_b + \theta_r) \\ gl_c m_l sin(\theta_b + \theta_l) \end{bmatrix}, \quad (17)$$

$$\mathbf{E} = \begin{bmatrix} 0 & 0 \\ 1 & 0 \\ 0 & 1 \end{bmatrix}, \quad (18)$$

where

$$m_{11}(\mathbf{q}) = I_b + I_l + I_r + (b^2 m_l)/4 + (b^2 m_r)/4 + d^2 m_l + d^2 m_r + d_c^2 m_b + l_c^2 m_l + l_c^2 m_r - 2dl_c m_l cos(\theta_l) - 2dl_c m_r cos(\theta_r) - bl_c m_l sin(\theta_l) + bl_c m_r sin(\theta_r), \quad (19)$$

$$m_{12}(\mathbf{q}) = I_r + l_c^2 m_r - dl_c m_r cos(\theta_r) + \frac{bl_c m_r sin(\theta_r)}{2}, \quad (20)$$

$$m_{13}(\mathbf{q}) = I_l + l_c^2 m_l - dl_c m_l cos(\theta_l) - \frac{bl_c m_l sin(\theta_l)}{2}. \quad (21)$$

Note that the model of this planar pendulum does not consider the contribution of the other two joints of the shoulder and elbow to the system dynamics, but it is assumed that the arms adopt the fixed L-pose as indicated before (the effect of these joints over the controlled system will be discussed later). The inertia parameters and representative distances in Table 2 are given for this configuration of the arms.

3.4. State-space representation and motor modeling

The state vector of the self-stabilizing robot is chosen as:

$$\mathbf{x}(t) = [\theta_b(t), \ \theta_r(t), \ \theta_l(t), \ \dot{\theta}_b(t), \ \dot{\theta}_r(t), \ \dot{\theta}_l(t)]^\top. \quad (22)$$

Substituting (14)–(18) into (13) and considering (22), the state-space representation of the system is found:

$$\dot{\mathbf{x}}(t) = \begin{bmatrix} \dot{\theta}_b \\ \dot{\theta}_r \\ \dot{\theta}_l \\ \mathbf{M}^{-1}(\mathbf{q})(\mathbf{E}\tau - \tau_f - \mathbf{c}(\mathbf{q}, \dot{\mathbf{q}}) - \mathbf{g}(\mathbf{q})) \end{bmatrix}. \quad (23)$$

The input signal to the state-space model (23) is a torque vector; however, in practice, the control input is voltage to the servo direct-current (DC) motors. The model of the servo DC motors should be considered in the modeling to reduce the gap between the simulation and the experiment.

Neglecting the electric inductance ($L_m = 0.0002\ [H] \approx 0$, according to the datasheet), the torque output of a DC motor is [40]:

$$\tau_i(t) = \frac{\eta_m \eta_g K_t k_g}{R_m} v_i(t) - \frac{\eta_m \eta_g K_t K_m k_g^2}{R_m}\dot{\theta}_i(t), \quad (24)$$

for $i = \{r, l\}$, where $v(t)$ [V] is voltage input of the DC motor, η_m, η_g are motor and gearbox efficiency constants, R_m [Ω] is armature resistance, K_t [N m/A] is motor torque constant, K_g is gearbox ratio, and K_m [Vs/rad] is motor voltage constant. All these parameters of the DC motor are obtained from the datasheet of the manufacturer (FAULHABER 2224-012 SR).

The servo actuators of the arms implement internally a proportional integral derivative (PID) controller with position and velocity feedback [54]:

$$v_i(t) = -K_P(\theta_i - \theta_{i,des}) - K_D(\dot{\theta}_i - \dot{\theta}_{i,des}) - K_I \int_0^t (\theta_i - \theta_{i,des})d\tau, \quad (25)$$

where K_P, K_D, K_I are proportional, derivative, and integral control gains, and $\theta_{i,des}$ is the reference input of the system.

Substituting (25) into (24) and closing the loop for the system (23) makes the user have to apply a reference angle for the motors with speed mode control of the servo. For the complex stabilization problem, PID works; however, the range of allowable initial conditions

is limited to an area close to the equilibrium point. In this work, the implementation of a non-linear optimal controller is intended to expand the stabilization range and also enhance the control performance.

To fulfill the task, it is assumed that the system is controlled by DC motors. Therefore, Eq. (24) is substituted into the state-space model (23):

$$\dot{\mathbf{x}}(t) = \begin{bmatrix} \dot{\theta}_b \\ \dot{\theta}_r \\ \dot{\theta}_l \\ \mathbf{M}^{-1}(\mathbf{q})(\mathbf{E}_s \mathbf{v} - \tau_f - \mathbf{c}(\mathbf{q}, \dot{\mathbf{q}}) - \mathbf{g}(\mathbf{q}) - \mathbf{U}_b \dot{\mathbf{q}}) \end{bmatrix}, \tag{26}$$

where

$$\mathbf{U}_b = \mathrm{diag}\left(0 \ , \ \frac{\eta_m \eta_g K_t K_m k_g^2}{R_m} \ , \ \frac{\eta_m \eta_g K_t K_m k_g^2}{R_m} \right), \tag{27}$$

and

$$\mathbf{E} = \begin{bmatrix} 0 & 0 \\ \frac{\eta_m \eta_g K_t k_g}{R_m} & 0 \\ 0 & \frac{\eta_m \eta_g K_t k_g}{R_m} \end{bmatrix}, \quad \mathbf{v}(t) = \begin{bmatrix} v_r(t) \\ v_l(t) \end{bmatrix}. \tag{28}$$

Now the state vector is measured and controlled by the input voltage of the DC motors. The voltage signal $v(t)$ that controls the DC motors within the range $[0, v_{max}]$ [V] is mapped into a PWM signal in the range $[0, 1]$ to express the normalized speed between zero and the maximum angular speed of the servo [52]. This was an approach to implement closed-loop control of servo-DC motors. Note that the negative range $[-v_{max}, 0]$ is mapped to $[-1, 0]$. This approach provides the matrix–vector implementation of the control with the contribution of all states to shape the control signal. The control signal is then converted into a velocity reference for the joint actuator multiplied by a constant factor. In particular, the Herkulex servos employed on the dual arm allow velocity control as they integrate high-resolution magnetic encoders at the motor side to measure the speed.

4. Controller design

4.1. Practical considerations

The SDRE controller described in the next subsection can be applied in two ways: (1) simultaneously with the manipulation task, involving the motion of the positioning joints (θ_1^i, θ_3^i, and θ_4^i) while exploiting the kinematic redundancy of the shoulder joints ($\theta_2^1 = \theta_l$, $\theta_2^2 = \theta_r$) for this purpose, or (2) separately from the manipulation task, correcting the orientation deviations caused by any endogenous or exogenous perturbation by using only θ_l and θ_r while the arms adopt a fixed nominal pose with the other joints. In the first case, a decoupled approach is followed in the design of the controller to avoid the real-time computation of the complete 9-DOF dynamics of the system, relying on the robustness of the SDRE controller to overcome the variations in the inertia parameters and the reaction wrenches caused by the other joints, considered as perturbations. In the second case, the controller should be able to overcome certain variations in the inertia parameters or mass distribution due to possible changes in the nominal pose of the arms, as well as other disturbances such as wind gusts or the aerodynamic downwash effect when the manipulator is deployed or retrieved by the aerial platform. Nevertheless, in normal operation conditions, the overall center of mass of the dual-arm robot will be under the contact point of the rolling base, which ensures the intrinsic stability of the platform. Experimental results presented in Section 6 will compare the performance of the controller to variations in the inertia parameters, as well as its response to simultaneous motions in the other joints.

4.2. SDRE controller

The SDRE methodology begins with the consideration of a class of nonlinear affine-in-input systems in the form of:

$$\dot{\mathbf{x}} = \mathbf{A}(\mathbf{x})\mathbf{x} + \mathbf{B}(\mathbf{x})\,\mathbf{v}, \tag{29}$$

where $\mathbf{x} \in \mathbb{R}^n$ is the state-vector and $\mathbf{v} \in \mathbb{R}^m$ is the input vector. $\mathbf{A}(\mathbf{x})$: $\mathbb{R}^n \rightarrow \mathbb{R}^{n \times n}$ and $\mathbf{B}(\mathbf{x})$: $\mathbb{R}^n \rightarrow \mathbb{R}^{n \times m}$ are state-dependent coefficient (SDC) parameterization of the dynamical system (26). The cost functional integral of the optimal control is [55]:

$$J = \frac{1}{2} \int_0^\infty \{\mathbf{x}^\top \mathbf{Q}(\mathbf{x})\mathbf{x} + \mathbf{v}^\top \mathbf{R}(\mathbf{x})\mathbf{v}\} dt, \tag{30}$$

where $\mathbf{Q}(\mathbf{x})$: $\mathbb{R}^n \rightarrow \mathbb{R}^{n \times n}$ and $\mathbf{R}(\mathbf{x})$: $\mathbb{R}^n \rightarrow \mathbb{R}^{m \times m}$ are the weighting matrices for states and inputs respectively, both of them symmetric and positive. $\mathbf{Q}(\mathbf{x})$ is semi-definite and $\mathbf{R}(\mathbf{x})$ is definite. The following conditions must be held to have a solution to the Riccati equation [47]:

1. $[\mathbf{A}(\mathbf{x})\mathbf{x}]$ and $[\mathbf{B}(\mathbf{x})\mathbf{v}]$ are piecewise-continuous vector-valued functions that satisfy the Lipschitz condition.
2. The pair of $(\mathbf{A}(\mathbf{x}), \mathbf{B}(\mathbf{x}))$ is a completely controllable representation of the system (29) for all $\mathbf{x} \in \mathbb{R}^n$.
3. The pair of $(\mathbf{A}(\mathbf{x}), \mathbf{Q}^{\frac{1}{2}}(\mathbf{x}))$ is a completely observable pair of the system (29) and the Cholesky decomposition of the state-weighting matrix in (30) for all $\mathbf{x} \in \mathbb{R}^n$.

The SDRE control law is in the form of:

$$\mathbf{v} = -\mathbf{R}^{-1}\mathbf{B}^\top(\mathbf{x})\mathbf{K}(\mathbf{x})\mathbf{x}, \tag{31}$$

where $\mathbf{K}(\mathbf{x})$: $\mathbb{R}^n \rightarrow \mathbb{R}^{n \times n}$ is the symmetric positive definite solution to the Riccati equation:

$$\mathbf{A}^\top(\mathbf{x})\mathbf{K}(\mathbf{x}) + \mathbf{K}(\mathbf{x})\mathbf{A}(\mathbf{x}) - \mathbf{K}(\mathbf{x})\mathbf{B}(\mathbf{x})\mathbf{R}^{-1}\mathbf{B}^\top(\mathbf{x})\mathbf{K}(\mathbf{x}) + \mathbf{Q}(\mathbf{x}) = \mathbf{0}. \tag{32}$$

Based on the final state-space representation in Eq. (26), the SDC matrices are found as:

$$\mathbf{A}(\mathbf{x}) = \begin{bmatrix} \mathbf{0}_{3 \times 3} & \mathbf{I}_{3 \times 3} \\ -\mathbf{M}^{-1}(\mathbf{x})\mathbf{G}(\mathbf{x}) & -\mathbf{M}^{-1}(\mathbf{x})[\mathbf{C}(\mathbf{x}) + \mathbf{D}_f + \mathbf{U}_b] \end{bmatrix}, \tag{33}$$

$$\mathbf{B}(\mathbf{x}) = \begin{bmatrix} \mathbf{0}_{3 \times 3} \\ \mathbf{M}^{-1}(\mathbf{x}) \end{bmatrix} \mathbf{E}_s. \tag{34}$$

where $\mathbf{D}_f = \mathrm{diag}(d_b, d_r, d_l)$, and also $\mathbf{g}(\mathbf{q}) = \mathbf{G}(\mathbf{q})\mathbf{q}$ and $\mathbf{c}(\mathbf{q}, \dot{\mathbf{q}}) = \mathbf{C}(\mathbf{q}, \dot{\mathbf{q}})\dot{\mathbf{q}}$ are held; note that $(\mathbf{q}, \dot{\mathbf{q}}) \in \mathbf{x}$.

Solution method: The solution to the Riccati equation (32) is based on the Hamiltonian matrix and the Schur decomposition approach [56]. The first step is to form the Hamiltonian matrix:

$$\mathbf{H}(\mathbf{x}) = \begin{bmatrix} \mathbf{A}(\mathbf{x}) & -\mathbf{B}(\mathbf{x})\mathbf{R}^{-1}\mathbf{B}^\top(\mathbf{x}) \\ -\mathbf{Q}(\mathbf{x}) & -\mathbf{A}^\top(\mathbf{x}) \end{bmatrix}. \tag{35}$$

The orthogonal transformation $\mathbf{\Gamma}(\mathbf{x})$ must be found in a way to transform $\mathbf{H}(\mathbf{x})$ in (35) into:

$$\mathbf{\Gamma}^\top(\mathbf{x})\mathbf{H}(\mathbf{x})\mathbf{\Gamma}(\mathbf{x}) = \begin{bmatrix} \mathbf{\Pi}_{11}(\mathbf{x}) & \mathbf{\Pi}_{12}(\mathbf{x}) \\ \mathbf{0} & \mathbf{\Pi}_{22}(\mathbf{x}) \end{bmatrix}, \tag{36}$$

where the eigenvalues of $\mathbf{\Pi}_{11}(\mathbf{x})$ have negative real parts and eigenvalues of $\mathbf{\Pi}_{22}(\mathbf{x})$ have positive real parts. Then the solution is found by partitioning $\mathbf{\Gamma}(\mathbf{x})$ to four square blocks using the expression [56]:

$$\mathbf{K}(\mathbf{x}) = \mathbf{\Gamma}_{21}(\mathbf{x})\mathbf{\Gamma}_{11}^{-1}(\mathbf{x}), \tag{37}$$

for the sub-optimal control law (31).

4.3. Implementation

Control law given by Eq. (31) provides the voltage signal to be applied on the DC motors of the shoulder actuators to control the angular position of the base. However, since the servo actuators implement internally a position/velocity controller that must be interfaced, the

voltage signal is converted into an equivalent angular speed taken as input reference by the servo, relying upon the linear relationship of these magnitudes for DC motors.

For the computation of Eq. (31) it is first necessary to obtain the gain $\mathbf{K}(\mathbf{x})$ which is the solution to Eq. (32). The connection between the control design and the system dynamics is through $\{\mathbf{A}(\mathbf{x}), \mathbf{B}(\mathbf{x})\}$ matrices which include the nonlinearity of the model, coupling of the states, and model of the actuators. So, proper selection of weighting matrices $\mathbf{Q}$, $\mathbf{R}$, and SDC matrices will result in a solution to the SDRE.

In order to implement the controller online for experimentation, the first step is to program SDC and Hamiltonian matrices $\{\mathbf{A}(\mathbf{x}), \mathbf{B}(\mathbf{x})\}$ and $\mathbf{H}(\mathbf{x})$ inside the control loop which is updated in each sampling time by state feedback, obtaining the joint position $\theta_r(t), \theta_l(t)$ and speed $\dot{\theta}_r(t), \dot{\theta}_l(t)$ from the servo encoders, whereas $\theta_b(t)$ and $\dot{\theta}_b(t)$ are measured with the IMU. Then, using C language and the LAPACK library, $\boldsymbol{\Gamma}_{11}(\mathbf{x}), \boldsymbol{\Gamma}_{12}(\mathbf{x})$ and $\boldsymbol{\Gamma}_{22}(\mathbf{x})$ matrices are found. The coding is done to perform this orthogonal transformation at each time step. The rest of the implementation is straightforward using Equation (37) and closing the loop by the control law (31).

Practical implementation of the SDRE has been reported in [57, 58], using MATLAB software and Arduino digital board limited to 20 Hz. Programming directly in C using the LAPACK library allows reducing the computational time to 1 ms on a Raspberry Pi board, as demonstrated in the experimental results. Wang et al. applied the SDRE controller experimentally on a multi-motor driving system using C++ language; however, Taylor series expansion was used to avoid solving the SDRE online [59]. Kazemi et al. also implemented the SDRE experimentally on a ring-shaped soft pneumatic actuator mimicking gastric pathologic motility conditions. The implementation sampling times were reported for three cases of 0.05, 0.5, 1 Hz [60].

5. System description

5.1. Anthropomorphic dual-arm rolling robot

The manipulator developed to perform the installation of clip-type bird flight diverters on the power line, depicted in Fig. 5, is a novel light-weight and compliant, anthropomorphic dual-arm system derived from our previous work [51,61], equipped with a rolling wheel to move along the line. This is a human-size and human-like dual-arm that implements the kinematic configuration described in [51], with four joints for end-effector positioning, three at the shoulder (flexion/extension, adduction/abduction, and lateral/medial rotation), and one at the elbow (flexion/ extension). The wrist orientation joints are not implemented to reduce the weight and inertia of the arms, or increase the effective payload, and because these are not necessary for the intended operation. The end-effector of the arms consists of a magnetic gripper (right arm) for grasping the device and an L-shaped hook (left arm) used to unlock the clamp of the clip-type bird diverter to be installed, as described in more detail in next subsection.

The manipulator is built with Herkulex smart servos and a customized frame structure manufactured in aluminum and carbon fiber. The left/right arm servos are connected through a serial interface to the Raspberry Pi computer board where the control program is executed. The orientation of the platform is measured by a BNO 055 inertial measurement unit (IMU) interfaced with an STM32F303K8 microcontroller board. The components and hardware architecture of the system are depicted in Fig. 6. The rolling base employs a pair of wheels (front and rear) attached to the shoulder structure, in such a way that the linear infrastructure is 30 mm under the baseline of the shoulder joints. The front wheel (3D printed, 60 mm diameter) is actuated by a servo in continuous rotation mode, whereas the rear wheel is a 6.5 mm diameter polymer pulley in free rotation. The robot includes a pair of U-shaped aluminum tubes (6 mm hollow section) attached to the base of the shoulder structure, used as a support frame. As stated in the introduction and described in Section 3, the joint that allows the adduction-abduction rotation of the shoulder will be considered redundant and used to maintain the equilibrium of the robot while perching on the linear infrastructure.
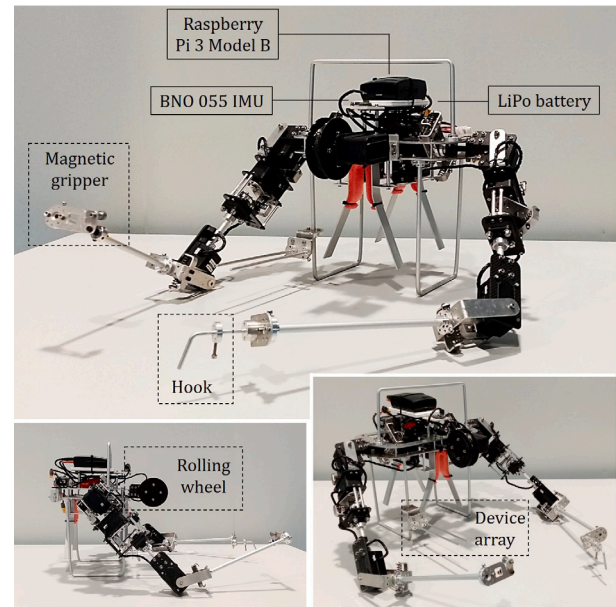

Fig. 5. Dual-arm equipped with magnetic gripper (right arm), hook (left arm), rolling wheel, and IMU to install the clip-type bird diverters.
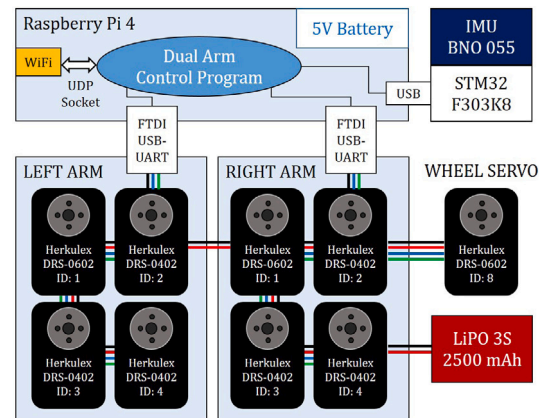

Fig. 6. Components and architecture of the dual-arm rolling robot.

5.2. Device installation procedure

The device to be installed on the power line mockup is a customized bird diverter consisting of a Wolfcraft microfix spring clamp and a 10 cm length orange rubber strip. This is shown in Fig. 5. The clamp is closed by default due to the action of a torsion spring, so a U-shaped aluminum rod is used as a lock to preload the clamp. The lock can be easily removed by applying a relatively small force around 5 N downwards with a hook, avoiding in this way the need for heavy actuators to perform the installation. The devices are initially loaded by an operator on the array attached to the support frame of the arms (see Fig. 7). The two holes on the handles of the clamp facilitate the extraction of the device along the parallel rods, exploiting the steel screw of the clamp mechanism to grasp the device with a magnet used as an end-effector for the right arm. The installation procedure can be seen in the video attachment or in the link [62].

5.3. Aerial deployment with multirotor platform

The very low weight (3.2 kg) of the dual-arm rolling robot allows its aerial transportation and deployment on high-altitude workspaces like
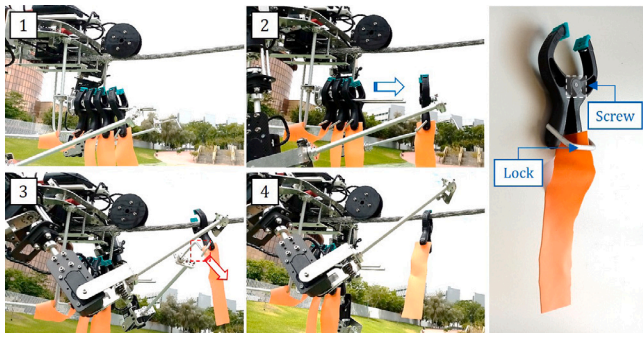
Fig. 7. The sequence of images showing the installation of the clip-type bird diverter. (1) The right arm grasps the device with the magnetic gripper. (2) The right arm retrieves the device. (3) The left arm removes the lock with the hook. (4) The device is installed.
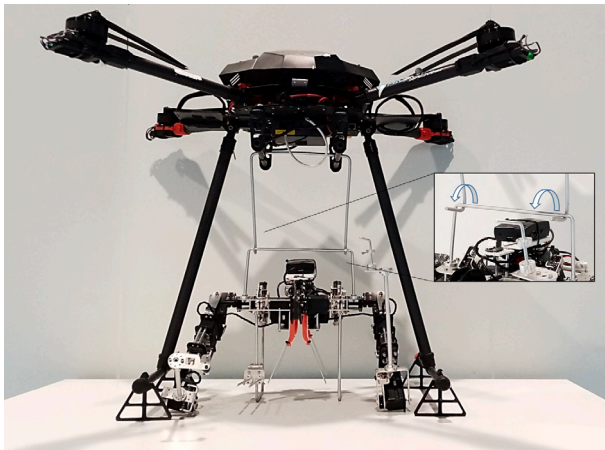

Fig. 8. Dual-arm rolling robot integrated on a multirotor platform with a double hook mechanism that facilitates the detachment in the aerial deployment.

power lines using medium size multirotor platforms, avoiding the need for human workers to carry the robot with them, or following conventional methods involving heavy platforms [14]. Fig. 8 shows a picture of the arms integrated on a Proskytec LRM quadrotor, representing in Fig. 9 a sequence of images from the video attachment that illustrates the operation. The detachment of the arms from the aerial platform is achieved with a simple handle-hook mechanism, in such a way that the hook keeps the arms attached due to their weight, but when these are supported by the linear infrastructure, the load is released from the hooks so the platform can be detached. To facilitate the insertion of the arms in the power line, the lower part of the shoulder structure incorporates two V-shaped frames that tend to align the cable with the wheeled base, while the hook provides a passive accommodation in pitch. The flight experiments were conducted in an indoor testbed in a representative scenario with a section of the power line. The platform, equipped with a CUAV v5 autopilot running Arducopter 3.6.1, was controlled by a human pilot in stabilizing (attitude) mode. The deployment operation in outdoors can be seen in the video attachment or the link [62].

6. Simulation and experimental results

6.1. Experimental identification of oscillation

The purpose of this first experiment is threefold: (1) identify experimentally the effect of the shoulder roll servo of the arms over the roll angle of the base, (2) determine experimentally parameters of interest
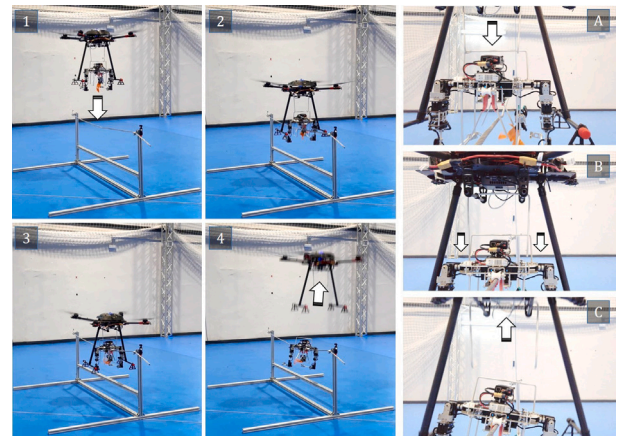

Fig. 9. Sequences of images from the video illustrating the aerial deployment of the dual-arm rolling robot on a power line testbed.
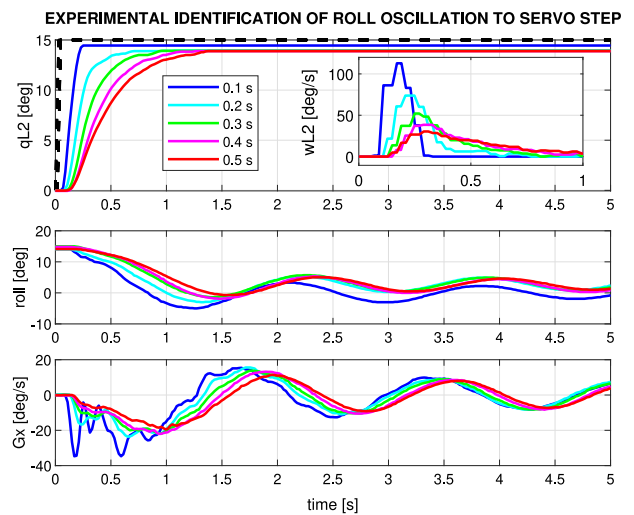

Fig. 10. Shoulder roll servo position/speed reference (up), roll angle of the base (middle), and X-axis angular speed (down) for different playtime values of the servo.

as the natural frequency and oscillation damping, (3) validate the dynamic model of the system and the actuator developed in Section 3 as the previous step to the evaluation of the controller in next subsections. To do that, a 15 deg amplitude step signal is applied as position reference to the shoulder roll servo of the left arm, varying the playtime parameter (the time required to reach the reference) from 0.1 to 0.5 s. Fig. 10 shows the measured servo position and speed along with the evolution of the roll angle and roll rate of the robot base, measured by the IMU.

6.2. Simulation of self-stabilizing system

The goal of this experiment is to validate the SDRE control designed in Section 4 using the model derived in Section 3, and compare its performance w.r.t. an LQR. The simulation is conducted assuming an initial deviation on the platform in roll, with zero velocity, that is, $\mathbf{x}(0) = [0.4, 0.1, -0.1, 0, 0, 0]^{\top}$. This corresponds to a situation in which the robot is deployed on the power line with an initial deviation in the roll angle. The final condition is the equilibrium point zero for all states. The control parameters are $\mathbf{Q} = diag(100, 0.01, 0.01, 50, 0, 0)$ and $\mathbf{R} =$
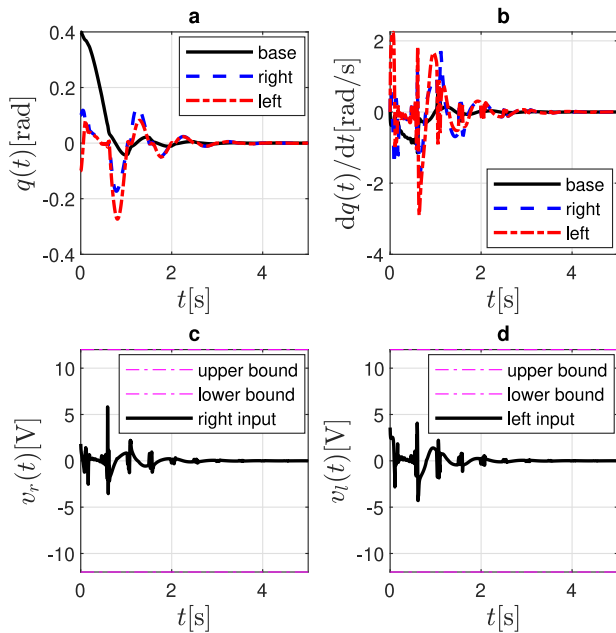
Fig. 11. States and inputs: (a) Angular position; (b) velocities of the stabilizer; (c) the input signal of the right arm; (d) input of the left arms.
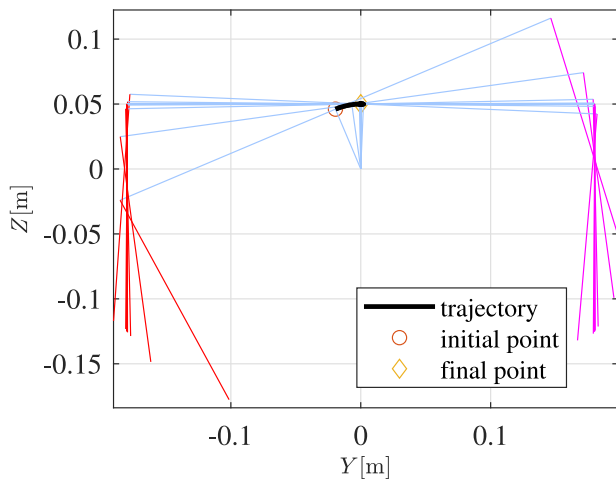

Fig. 12. Configuration of the stabilizer in regulation control.

Fig. 13. The comparison between the SDRE and LQR for stabilization of the system for $\theta_b(0) = 0.55$ rad and $\theta_b(0) = 0.8$ rad.

Fig. 14. The simulation result for different initial conditions covering the workspace of $\theta_b(t)$.

6.3. Experimental results of self-stabilization

The SDRE and LQR controllers have been implemented in C language on the Raspberry Pi computer board and tested on the anthropomorphic rolling robot described in Section 5, using the LAPACK library for computing the inverse matrices and the Schur factorization required in the resolution of the Riccati equations. The control rate is set to 50 Hz, determined by the interface of the servo actuators (higher rates may lead to repeated samples). In the experiment, the robot is deployed in the power line testbed with initial state $\mathbf{x}(0) = [0.3, 0, -0.25, 0, 0, 0]^\top$. Fig. 15 compares the evolution of the platform for both controllers, representing the angle of the base along with the rotation angle of the left–right arms. As can be seen, the SDRE controller reaches faster the desired equilibrium point with smaller position deviations in the arm joints.

According to the controller (31), the states of the system converge to zero when time goes to infinity, as indicated in Figs. 11 and 13 as well. However, the behavior of the controlled system in the real experiments is slightly different as the servo actuators of the dual-arm rolling robot introduce certain effects such as communication delays due to the serial interface (around 5 ms), the dynamics of the embedded position/speed controller, a certain backlash or clearance in the joints, or errors in the angular position measurement of the servo actuator. These devices incorporate an incremental encoder at the motor side (before the gearbox) that allows to obtain accurate speed measurements, whereas the absolute position of the output shaft is obtained from an analog potentiometer that may present small errors. In practice, a minimum value should be considered for the angular position error of the base to stop the control task when it reaches this bound.

6.4. SDRE performance evaluation

To simplify the controller design (see Section 4), the planar stabilization dynamics described in Sections 3.2 and 3.3 was decoupled from the overall 3D dynamics of the dual arm rolling robot in which

$I_{2\times2}$. The generalized coordinates of the system are shown in Fig. 11-a and b. The input signals for the right and left arms are illustrated in Fig. 11-c and d. The configuration of the system in the regulation mode is shown in Fig. 12. The SDRE successfully regulated the system to the equilibrium point. A small overshoot is recommended for stabilization of the pendulum-like systems [47]; which can be seen in Fig. 11-a. This means the system could freely jump over the equilibrium point and then come back again which emulates a fast response. Lack of overshoot implies that the system should always stay behind the equilibrium point (a slow response). The performance of the SDRE nonlinear control has been compared with the LQR for different initial values. Fig. 13 represents the evolution of the system when the initial roll deviation of the base increases to $\theta_b(0) = 0.55$ rad. It can be seen that the LQR fails to regulate to the equilibrium point for higher values $\theta_b(0) = 0.8$ rad, while the SDRE performs successfully, as it can be seen in Fig. 13. A series of simulations have been also performed for a variety of the initial points in the workspace to ensure the success of the controller. These simulation results are shown in Fig. 14.
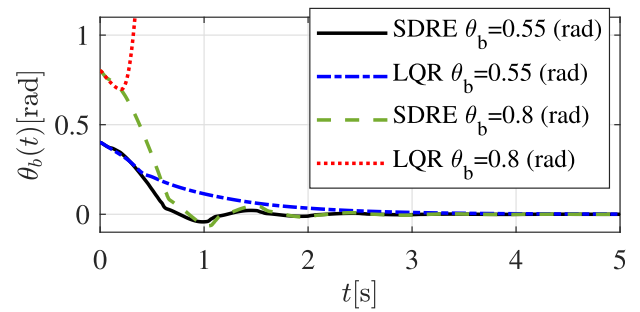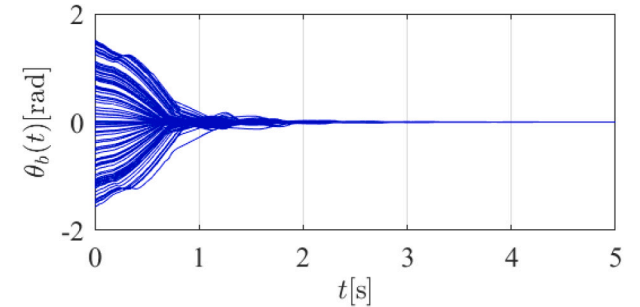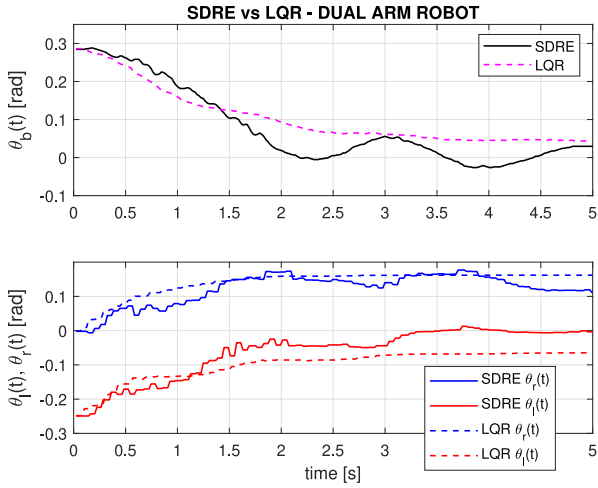
Fig. 15. Angular position of the base (up) and the links (down) of the LQR and SDRE controllers implemented on the dual-arm rolling robot.

Fig. 16. Compared performance of the SDRE controller to three poses of the arms changing the inertia: nominal L-pose (normal line), forearm stretched (dashed line, increased inertia), and L-posed with upper arm lifted 10 degrees (dot-dash line, reduced inertia).

the installation procedure is executed. This is possible since the stabilization plane is orthogonal to the longitudinal direction of the linear infrastructure and because the manipulator provides one redundant joint at the shoulder that can be devoted to the stabilization while the rest of servo actuators are used for the manipulation task. The planar model in Fig. 4 considers only the upper arm link since its mass is significantly higher compared to the forearm link due to the mechanical construction, although its inertia properties and CoM position (l, l_c, I_r and I_l in the model) will depend of the angular position of the other joints. In order to evaluate the robustness of the SDRE controller against variations or uncertainty in the estimation of these parameters, Fig. 16 evaluates the evolution of the manipulator base from an initial deviation around 10 degrees for different poses of the arms, considering three cases: nominal pose of the arms with the forearm lifted 90 degrees (L pose), forearm stretched (higher inertia), and arms in L pose with 10 degrees elevation in the shoulder pitch joint (lower inertia). As it can be seen, the controller is able to stabilize correctly the base, although the rise time is increased around 0.3 s in the two last cases, and the setting time is higher for the pose with higher inertia.

The effectiveness of the SDRE controller to stabilize the orientation of the manipulator base using the shoulder roll joints of the arms ($\theta_2^1 = \theta_l$ and $\theta_2^2 = \theta_r$ in Figs. 3 and 4) while the other three joints (θ_1, θ_2, θ_3) are moving has been validated with the experiment illustrated in Fig. 17. Note that the motion of these three joints is considered as perturbations since the controller design is decoupled from the complete dynamics of the dual arm rolling robot, as mentioned before. A sinusoidal reference with 0.25 Hz frequency and amplitude 10, 20 and 20 degrees respectively is generated for the three joints of both arms. Fig. 17 evidences the oscillation induced due to the dynamic coupling and the bias in the orientation due to the unbalanced mass distribution on the base when the controller is disabled, as well as the ability of the SDRE to overcome both effects.

The response of the controller to external perturbations in the form of pushing/pulling forces exerted by hand over the base are shown in Fig. 18 along with the execution time of the implemented SDRE algorithm on the three tests. The mean time for the first test is 0.942 ms, with standard deviation 0.083 ms, executing the C/C++ implementation of the SDRE relying on the LAPACK library on a Raspberry Pi Model 3. Note that the update rate of the control loop is set to 50 Hz (20 ms period) since the servo actuator may provide repeated samples at rates above 70 Hz.
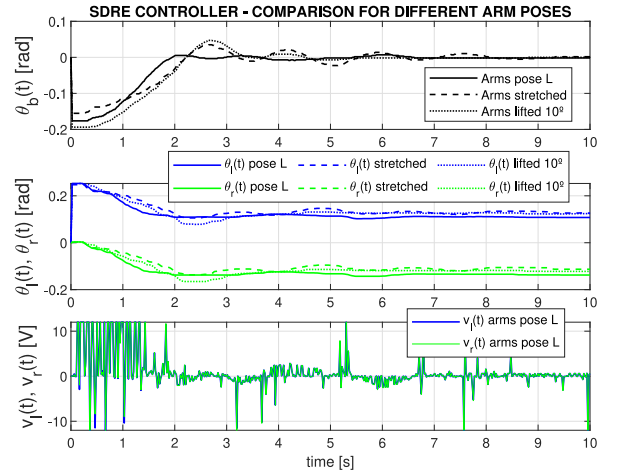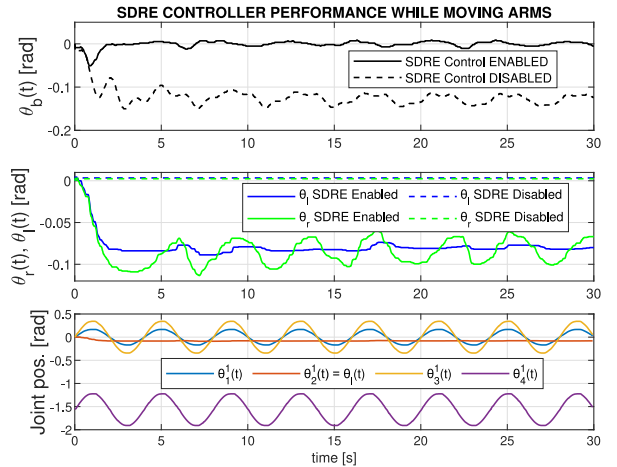

Fig. 17. Influence of the dynamic coupling caused by the rotation of the shoulder (θ_1, θ_3) and elbow (θ_4) joints on the manipulator base, showing the effectiveness of the SDRE controller acting on θ_2. The bias in the orientation of the base is due to the mass unbalance in the construction of the arms.

6.5. Experimental results of installation on power line

The procedure described in Section 5.2 is validated in this section through the installation of four customized clip-type bird diverters. The phases of this bimanual operation (depicted in Fig. 7) are indicated in Table 3, representing in Figs. 19 and 20 the trajectories of the tool center point (TCP) of both arms. As it can be seen in these figures, the trajectories are the same on each iteration, except for the variation in the X-axis coordinate of the right arm in phase 1 (see Table 3), corresponding to the grasping of the devices from the array. Once the device is installed, the platform rolls backward along the power line toward the next installation point. The operation time is 8 s per device.

6.6. Rolling base performance

The goal of this experiment is to evaluate the energy consumption of the rolling base for different reference speeds and angles of inclination
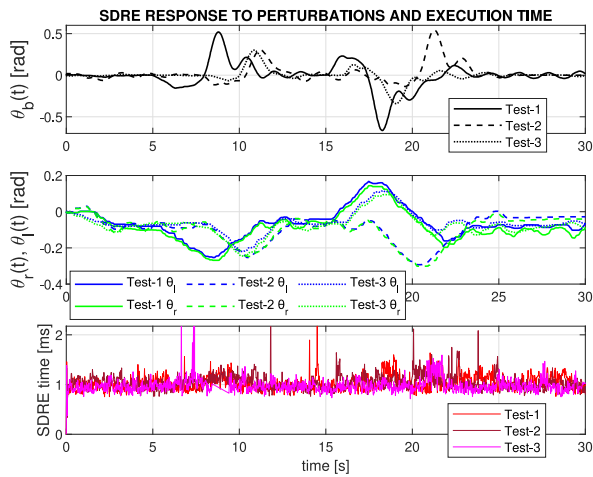
Fig. 18. Evolution of angular position of the base for three different experiments illustrating the response of the SDRE controller to external pushing/pulling forces exerted manually as perturbations. Execution time of the SDRE controller (bottom).

Table 3
Phases involved in the installation of the device with the dual-arm.

–	Left arm	Right arm
1	Approach to power line	Grasp device with magnetic gripper
2	Approach to device	Retrieve device from linear array
3	Insert hook on lock	Put clamp around the power line
4	Remove lock (impulse)	Release clamp from gripper
5	Retract arm	Retract arm

Fig. 21. Rolling base performance for different speeds and pitch angles.
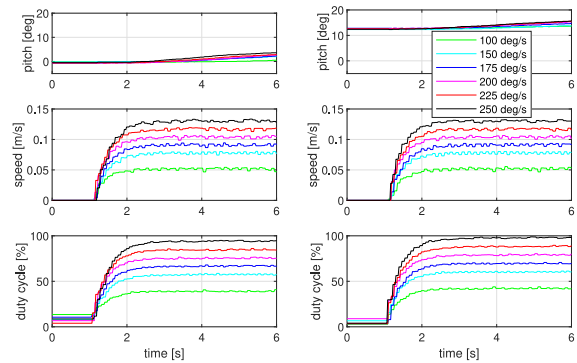
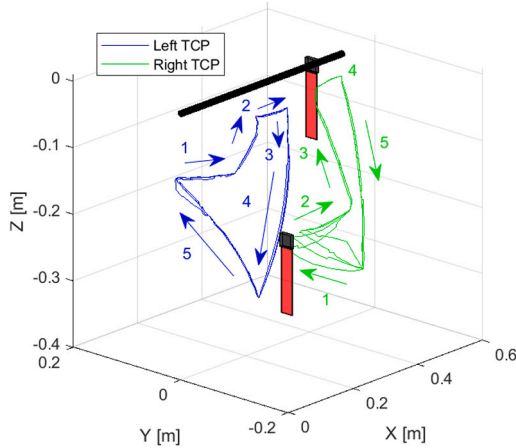**Fig. 22.** Evolution of the rolling base for 0 and 12 deg pitch.

Fig. 19. The 3D trajectory of the left/right TCPs (tool center points) during the installation of the four clip-type bird flight diverters on the power line.
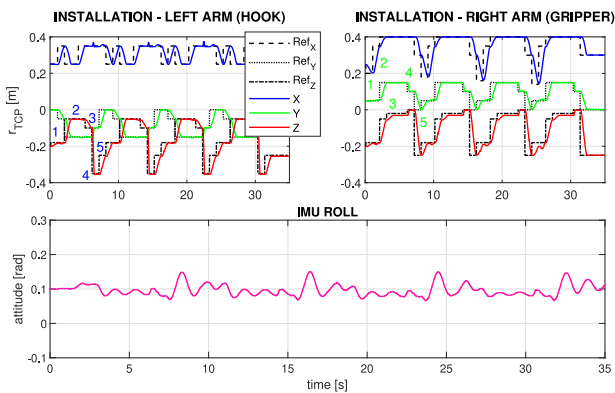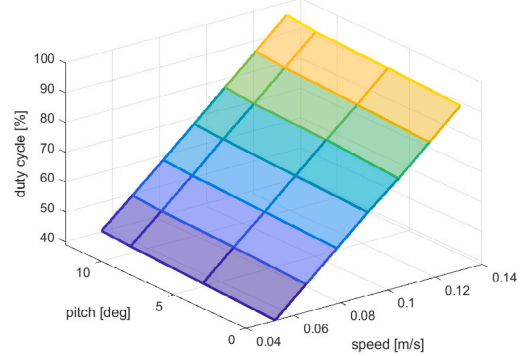

Fig. 20. Evolution of the left/right TCPs (up), and perturbation in the roll angle measured by the IMU (down).

(pitch angle) to account for the power line sag. For this purpose, the Herkulex DRS-0602 servo used to drive the 60 mm section wheel will be commanded in speed, specifying values from 100 to 250 deg/s with increments of 25 deg/s, taking the PWM signal as a representative metric of the mean current injected to the motor. Fig. 21 collects the mean PWM values for four inclination angles: 0, 5, 10, and 12 deg. Inclination angles above 15 degrees tend to cause wheel slippage, so the friction force of the rolling base can be estimated from the mass of the robot around 7.5 N. Fig. 21 evidences a linear increment of the PWM with the reference speed, and a negligible variation with the inclination angle of the line since the internal friction of the gearbox (200:1 ratio) is more significant than the increment in torque required to compensate the slope. This can be appreciated in Fig. 22, comparing the measurements for 0 and 12 deg inclination angles. The slight variation of the pitch angle in both cases is due to the deflection of the cable when the robot is at the midpoint of the support structure.

7. Conclusion

In this work, a novel lightweight-compliant anthropomorphic dual arm system with a rolling base is developed for the realization of inspection and maintenance operations in linear infrastructures like

power lines or pipelines. The very low weight of the arms allows its aerial transportation and deployment on high-altitude workspaces using multirotor platforms. To fulfill the intended task, taking into account the lack of stable support points in these infrastructures, the robot needs to maintain the equilibrium of the platform over the line, designing and implementing for this purpose a self-stabilizing controller based on the state-dependent Riccati equation that accounts for the under-actuated dynamics. Simulation and experimental results reported success and the results of self-stabilization have been compared with classical LQR controllers. The comparison showed the LQR, as expected, was able to regulate the system close to the equilibrium point while the SDRE covered a wider range of initial conditions.

CRediT authorship contribution statement

Alejandro Suarez: Conceptualization, Writing, Prototype development, Experimentation, Data curation, Software development, Revision. **Saeed Rafee Nekoo:** Writing, Dynamic modeling, Controller design, Simulation results, Revision. **Anibal Ollero:** Project coordinator, Conceptualization, Funding, Revision.

Declaration of competing interest

The authors declare the following financial interests/personal relationships which may be considered as potential competing interests: Alejandro Suarez reports financial support and equipment, drugs, or supplies were provided by European Commission. Alejandro Suarez reports financial support and article publishing charges were provided by Spain Ministry of Science and Innovation. Alejandro Suarez reports financial support was provided by Consejería de Transformación Económica, Industria, Conocimiento y Universidades de la Junta de Andalucía (Spain). Authors declare no conflict of interest.

Data availability

C/C++ source code of SDRE and LQR controllers attached as Electronic Annex.

Acknowledgments

Appendix A. Supplementary data

Supplementary material related to this article can be found online at https://doi.org/10.1016/j.mechatronics.2023.103021.

References

[1] Ollero A, Tognon M, Suarez A, Lee D, Franchi A. Past, present, and future of aerial robotic manipulators. IEEE Trans Robot 2022;38(1):626–45. http://dx.doi.org/10.1109/TRO.2021.3084395.

[2] Meng X, He Y, Han J. Survey on aerial manipulator: System, modeling, and control. Robotica 2020;38(7):1288–317.

[3] Mohta K, Kumar V, Daniilidis K. Vision-based control of a quadrotor for perching on lines. In: 2014 IEEE international conference on robotics and automation. ICRA, 2014, p. 3130–6. http://dx.doi.org/10.1109/ICRA.2014.6907309.

[4] Mirallès F, Hamelin P, Lambert G, Lavoie S, Pouliot N, Montfrond M, Montambault S. LineDrone technology: Landing an unmanned aerial vehicle on a power line. In: 2018 IEEE international conference on robotics and automation. ICRA, 2018, p. 6545–52. http://dx.doi.org/10.1109/ICRA.2018.8461250.

[5] Popek KM, Johannes MS, Wolfe KC, Hegeman RA, Hatch JM, Moore JL, Katyal KD, Yeh BY, Bamberger RJ. Autonomous grasping robotic aerial system for perching (AGRASP). In: 2018 IEEE/RSJ international conference on intelligent robots and systems. IROS, 2018, p. 1–9. http://dx.doi.org/10.1109/IROS.2018.8593669.

[6] Sato T, Kominami T, Paul H, Miyazaki R, Ladig R, Shimonomura K. Passive perching and landing mechanism for multirotor flying robot. In: 2021 IEEE/ASME international conference on advanced intelligent mechatronics. AIM, 2021, p. 396–401. http://dx.doi.org/10.1109/AIM46487.2021.9517558.

[7] Suarez A, Caballero A, Garofano A, Sanchez-Cuevas PJ, Heredia G, Ollero A. Aerial manipulator with rolling base for inspection of pipe arrays. IEEE Access 2020;8:162516–32.

[8] Cacace J, Silva MD, Fontanelli GA, Lippiello V. A novel articulated rover for industrial pipes inspection tasks. In: 2021 IEEE/ASME international conference on advanced intelligent mechatronics. AIM, 2021, p. 1027–32. http://dx.doi.org/10.1109/AIM46487.2021.9517691.

[9] Bernard M, Kondak K, Maza I, Ollero A. Autonomous transportation and deployment with aerial robots for search and rescue missions. J Field Robotics 2011;28(6):914–31.

[10] Suarez A, Heredia G, Ollero A. Physical-virtual impedance control in ultra-lightweight and compliant dual-arm aerial manipulators. IEEE Robot Autom Lett 2018;3(3):2553–60. http://dx.doi.org/10.1109/LRA.2018.2809964.

[11] Suarez A, Real F, Vega VM, Heredia G, Rodriguez-Castano A, Ollero A. Compliant bimanual aerial manipulation: Standard and long reach configurations. IEEE Access 2020;8:88844–65.

[12] Lima JJ, Rocha RT, Janzen FC, Tusset AM, Bassinello DG, Balthazar JM. Position control of a manipulator robotic arm considering flexible joints driven by a DC motor and a controlled torque by a MR-brake. In: ASME international mechanical engineering congress and exposition, Vol. 50558. American Society of Mechanical Engineers; 2016, V04BT05A022.

[13] Lima JJ, Balthazar JM, Rocha RT, Janzen FC, Bernardini D, Litak G, Bassinello DG, Tusset AM. On positioning and vibration control application to robotic manipulators with a nonideal load carrying. Shock Vib 2019;2019.

[14] Power-Lines E. IEEE guide for maintenance methods on energized power-lines. IEEE Standard 516, 2009.

[15] Alhassan AB, Zhang X, Shen H, Xu H. Power transmission line inspection robots: A review, trends and challenges for future research. Int J Electr Power Energy Syst 2020;118:105862.

[16] Yang L, Fan J, Liu Y, Li E, Peng J, Liang Z. A review on state-of-the-art power line inspection techniques. IEEE Trans Instrum Meas 2020;69(12):9350–65.

[17] Pouliot N, Montambault S. Geometric design of the LineScout, a teleoperated robot for power line inspection and maintenance. In: 2008 IEEE international conference on robotics and automation. IEEE; 2008, p. 3970–7.

[18] Alhassan AB, Zhang X, Shen H, Jian G, Xu H, Hamza K. Investigation of aerodynamic stability of a lightweight dual-arm power transmission line inspection robot under the influence of wind. Math Probl Eng 2019;2019.

[19] Gao Y, Song G, Li S, Zhen F, Chen D, Song A. LineSpyX: A power line inspection robot based on digital radiography. IEEE Robot Autom Lett 2020;5(3):4759–65.

[20] Iversen N, Kramberger A, Schofield OB, Ebeid E. Pneumatic-mechanical systems in uavs: Autonomous power line sensor unit deployment. In: 2021 IEEE international conference on robotics and automation. ICRA, IEEE; 2021, p. 548–54.

[21] Suarez A, Salmoral R, Zarco-Periñan PJ, Ollero A. Experimental evaluation of aerial manipulation robot in contact with 15 kV power line: Shielded and long reach configurations. IEEE Access 2021;9:94573–85.

[22] Nekovář F, Faigl J, Saska M. Multi-tour set traveling salesman problem in planning power transmission line inspection. IEEE Robot Autom Lett 2021;6(4):6196–203. http://dx.doi.org/10.1109/LRA.2021.3091695.

[23] Rodriguez-Castaño A, Nekoo SR, Romero H, Salmoral R, Acosta JÁ, Ollero A. Installation of clip-type bird flight diverters on high-voltage power lines with aerial manipulation robot: Prototype and testbed experimentation. Appl Sci 2021;11(16):7427.

[24] Chang W, Yang G, Yu J, Liang Z, Cheng L, Zhou C. Development of a power line inspection robot with hybrid operation modes. In: 2017 IEEE/RSJ international conference on intelligent robots and systems. IROS, IEEE; 2017, p. 973–8.

[25] Mirallès F, Hamelin P, Lambert G, Lavoie S, Pouliot N, Montfrond M, Montambault S. LineDrone technology: Landing an unmanned aerial vehicle on a power line. In: 2018 IEEE international conference on robotics and automation. ICRA, IEEE; 2018, p. 6545–52.

[26] Richard P-L, Pouliot N, Morin F, Lepage M, Hamelin P, Lagac M, Sartor A, Lambert G, Montambault S. Lineranger: Analysis and field testing of an innovative robot for efficient assessment of bundled high-voltage powerlines. In: 2019 international conference on robotics and automation. ICRA, IEEE; 2019, p. 9130–6.

[27] Hrabar S, Merz T, Frousheger D. Development of an autonomous helicopter for aerial powerline inspections. In: 2010 1st international conference on applied robotics for the power industry. IEEE; 2010, p. 1–6.

[28] Wang B, Chen X, Wang Q, Liu L, Zhang H, Li B. Power line inspection with a flying robot. In: 2010 1st international conference on applied robotics for the power industry. IEEE; 2010, p. 1–6.

[29] Cacace J, Orozco-Soto SM, Suarez A, Caballero A, Orsag M, Bogdan S, Vasiljevic E, Ebeid E, Rodriguez JAA, Ollero A. Safe local aerial manipulation for the installation of devices on power lines: AERIAL-CORE first year results and designs. Appl Sci 2021;11(13):6220.

[30] AERIAL-CORE project homepage. 2022, https://aerial-core.eu/, accessed: 2022-11-10.

[31] Yu L, Yang E, Ren P, Luo C, Dobie G, Gu D, Yan X. Inspection robots in oil and gas industry: a review of current solutions and future trends. In: 2019 25th international conference on automation and computing. ICAC, 2019, p. 1–6. http://dx.doi.org/10.23919/IConAC.2019.8895089.

[32] Kawaguchi Y, Yoshida I, Kurumatani H, Kikuta T, Yamada Y. Internal pipe inspection robot. In: Proceedings of 1995 IEEE international conference on robotics and automation, Vol. 1. 1995, p. 857–62. http://dx.doi.org/10.1109/ROBOT.1995.525390.

[33] Ab Rashid MZ, Yakub MFM, bin Shaikh Salim SAZ, Mamat N, Putra SMSM, Roslan SA. Modeling of the in-pipe inspection robot: A comprehensive review. Ocean Eng 2020;203:107206.

[34] Roslin NS, Anuar A, Jalal MFA, Sahari KSM. A review: Hybrid locomotion of in-pipe inspection robot. Procedia Eng 2012;41:1456–62.

[35] Valls Miro J, Ulapane N, Shi L, Hunt D, Behrens M. Robotic pipeline wall thickness evaluation for dense nondestructive testing inspection. J Field Robotics 2018;35(8):1293–310.

[36] García-Martín J, Gómez-Gil J, Vázquez-Sánchez E. Non-destructive techniques based on eddy current testing. Sensors 2011;11(3):2525–65.

[37] Rifai D, Abdalla AN, Razali R, Ali K, Faraj MA. An eddy current testing platform system for pipe defect inspection based on an optimized eddy current technique probe design. Sensors 2017;17(3):579.

[38] Ollero A, Heredia G, Franchi A, Antonelli G, Kondak K, Sanfeliu A, Viguria A, Martinez-de Dios JR, Pierri F, Cortés J, et al. The aeroarms project: Aerial robots with advanced manipulation capabilities for inspection and maintenance. IEEE Robot Autom Mag 2018;25(4):12–23.

[39] Dang P, Lewis FL. Controller for swing-up and balance of single inverted pendulum using SDRE-based solution. In: 31st annual conference of IEEE industrial electronics society, 2005. IECON 2005. IEEE; 2005, p. 6–pp.

[40] Nekoo SR. Digital implementation of a continuous-time nonlinear optimal controller: An experimental study with real-time computations. ISA Trans 2020;101:346–57.

[41] Peruzzi N, Chavarette FR, Balthazar JM, Tusset AM, Perticarrari ALPM, Brasil R. The dynamic behavior of a parametrically excited time-periodic MEMS taking into account parametric errors. J Vib Control 2016;22(20):4101–10.

[42] Tusset A, De Lima J, Janzen F, Junior J, Balthazar JM, Kossoski A, et al. A hybrid PID-LQR control applied in positioning control of robotic manipulators subject to excitation from non-ideal sources. In: Nonlinear vibrations excited by limited power sources. Springer; 2022, p. 393–403.

[43] Pearson J. Approximation methods in optimal control I. Sub-optimal control. Int J Electron 1962;13(5):453–69.

[44] Pérez J, Junghans S. Contraction region estimate for state-dependent riccati equation-based controllers and its application to a two-wheeled inverted pendulum. In: 2021 IEEE international conference on mechatronics. ICM, IEEE; 2021, p. 01–7.

[45] Ramos-Paz S, Ornelas-Tellez F, Inostroza-Moreno LA. Nonlinear optimal tracking control applied to the rotary inverted pendulum. In: 2021 IEEE international autumn meeting on power, electronics and computing, Vol. 5. ROPEC, IEEE; 2021, p. 1–5.

[46] Nekoo SR, Acosta JÁ, Heredia G, Ollero A. A PD-type state-dependent Riccati equation with iterative learning augmentation for mechanical systems. IEEE/CAA J Autom Sin 2022;9:1–13.

[47] Nekoo SR, Acosta JÁ, Heredia G, Ollero A. A benchmark mechatronics platform to assess the inspection around pipes with variable pitch quadrotor for industrial sites. Mechatronics 2021;79:102641.

[48] Samadikhoshkho Z, Ghorbani S, Janabi-Sharifi F. Modeling and nonlinear optimal control of N-rotor VTOL unmanned aerial vehicles. In: Proc. CSME congr., Vol. 3. 2020.

[49] Dos Santos GP, Kossoski A, Balthazar JM, Tusset AM. SDRE and LQR controls comparison applied in high-performance aircraft in a longitudinal flight. Int J Robot Control Syst 2021;1(2):131–44.

[50] Huifeng C, Hongxing L, Peipei Y. Swinging-up and stabilization of the inverted pendulum by energy well and SDRE control. In: 2009 Chinese control and decision conference. IEEE; 2009, p. 2222–6.

[51] Suarez A, Heredia G, Ollero A. Design of an anthropomorphic, compliant, and lightweight dual arm for aerial manipulation. IEEE Access 2018;6:29173–89.

[52] Korayem MH, Nekoo SR. Controller design of cooperative manipulators using state-dependent Riccati equation. Robotica 2018;36(4):484–515.

[53] Bird diverter installation. 2022, https://www.youtube.com/watch?v=0Iu20ZsuEI4, accessed: 2022-11-10.

[54] Wada T, Ishikawa M, Kitayoshi R, Maruta I, Sugie T. Practical modeling and system identification of R/C servo motors. In: 2009 IEEE control applications, (CCA) & intelligent control. ISIC, IEEE; 2009, p. 1378–83.

[55] Nekoo SR. Tutorial and review on the state-dependent Riccati equation. J Appl Nonlinear Dyn 2019;8(2):109–66.

[56] Laub A. A Schur method for solving algebraic Riccati equations. IEEE Trans Automat Control 1979;24(6):913–21.

[57] Nekoo SR, Acosta JÁ, Heredia G, Ollero A. A PD-type state-dependent Riccati equation with iterative learning augmentation for mechanical systems. IEEE/CAA J Autom Sin 2022;9(8):1499–511. http://dx.doi.org/10.1109/JAS.2022.105533.

[58] Nekoo SR. Digital implementation of a continuous-time nonlinear optimal controller: An experimental study with real-time computations. ISA Trans 2020;101:346–57.

[59] Wang M, Dong X, Ren X, Chen Q. SDRE based optimal finite-time tracking control of a multi-motor driving system. Internat J Control 2021;94(9):2551–63.

[60] Kazemi S, Stommel M, Cheng LK, Xu W. Finite-time contraction control of a ring-shaped soft pneumatic actuator mimicking gastric pathologic motility conditions. Soft Robot 2022.

[61] LiCAS robotic arms homepage. 2022, https://licas-robotic-arms.com/, accessed: 2022-11-10.

[62] Video of the experiments (online). 2022, https://www.youtube.com/watch?v=veLgvoTKBC4, accessed: 2022-11-15.

Alejandro Suarez is a postdoctoral researcher and assistant professor at University of Seville, Spain, in the GRVC Robotics Labs. He received the B.S. in Telecommunications in 2012, the M.Sc. degree in Automation Engineering in 2013, and the Ph.D. degree in Robotics in 2019 from the University of Seville, developing his research work in the same group since 2012. His Ph.D. thesis was awarded with the AIRBUS Aerospace Chair from the University of Seville, and with the Spanish/Portuguese Societies of Robotics (SEIDROB/SPR). He has participated in several aerial robotics projects funded by the European Commission, including FP7 EC-SAFEMOBIL, H2020 AEROARMS, H2020 HYFLIERS, H2020 AERIAL-CORE, and ERC Advanced Grant GRIFFIN, as well as in the European Robotics and Artificial Ingelligence Network (euROBIN). He has also participated in projects with companies involving technology transfer, particularly through the development and application of lightweight and compliant arms for service applications (LiCAS). He is author of more than 40 papers in journals and international conferences, including a survey paper in aerial robotic manipulation published in the IEEE Transactions on Robotics, becoming Associate Editor of this journal in 2023. He is also reviewer of several robotics journals and conferences, and has served as Program Chair for the ICUAS 2022. His current research interests include robotics, aerial and space robotic manipulation, robotic arm design, and compliance.

Saeed Rafee Nekoo is a senior postdoctoral research fellow with Robotics, Vision, and Control Research Group (GRVC) at the University of Seville in association with AICIA. He is currently involved in AERIAL-CORE H2020 project in the control of inspection robots for high-voltage power lines; and Advanced Grant GRIFFIN ERC in the design and prototyping of bird-shaped legs for perching; and lightweight cooperative manipulator design, prototyping, and control for a flapping bird bio-inspired robot. Saeed's research interest includes: robotics, nonlinear and optimal control, control engineering, manufacturing, cooperative robotics, flexible joint manipulators, observer, and estimator design, path planning, wheeled mobile robots, control of autonomous

underwater vehicles, free-floating space manipulator design, and control, digital implementation of continuous-time non-linear controllers, and design, manufacturing, and control of mechatronics systems, aerial robotics, multirotor UAV, variable-pitch-rotor quadcopter control, motion control of aerobatic maneuver, sliding mode control, the soft landing of drones, lightweight cooperative manipulators, gravity compensation.

Anibal Ollero is full Professor and Head of GRVC at University Seville, and Scientific Advisor of the Center for Aerospace Technologies (CATEC) also in Seville. He has been full professor at the Universities of Santiago and Malaga (Spain) and researcher at the Robotics Institute of Carnegie Mellon University (Pittsburgh, USA) and LAAS-CNRS (Toulouse, France). He authored more than 750 publications, including 9 books and 200 papers in journals and has been editor of 15 books. He has delivered plenaries and keynotes in more than 100 events including IEEE ICRA 2016 and IEEE IROS 2018. He has been supervisor or co-supervisor of 45 Ph.D. Thesis that have received many awards. He led more than 160 research projects, participating in more than 25 projects of the European Research Programmes being coordinator of 7 and associated or deputy coordinator of 3, all of them dealing with unmanned aerial systems and aerial robots. From November 2018 he is run-

ning the GRIFFIN ERC-Advanced Grant with the objective of developing a new generation of aerial robots that will be able to glide, flapping the wings, perch and manipulate by maintaining the equilibrium, and from December 2019 he is the coordinator of the H2020-AERiAL-CORE project with the participation of 15 universities, research centers and companies dealing with aerial robotic manipulators and applications to inspection and maintenance He has transferred technologies to more than 20 companies and has been awarded with 25 international research and innovation awards, including the recent Rei Jaume I in New Technologies (Spain), the Challenge 3 of the MBZIRC 2020 International Robotics Competition, the Overall Information and Communication Technologies Innovation Radar Prize 2017 of the European Commission, and has been also elected between the three European innovators of the year being candidate to the European personalities of the year 2017. He is IEEE Fellow ''for contributions to the development and deployment of aerial robots''. Currently co-chair of the ''IEEE Technical Committee on Aerial Robotics and Unmanned Aerial Vehicles'', coordinator of the ''Aerial Robotics Topic Group'' of euRobotics and has been member of the ''Board of Directors'' of euRobotics until March 2019. He has been also founder and president of the Spanish Society for the Research and Development in Robotics (SEIDROB) until November 2017.